CHEMISTRY OF MATERIALS

pubs.acs.org/cm

Article

Phase Behavior, Structural Dynamics, and Ionic Conductivity in Perhalogenated Lithium *Closo*-Dodecaborates

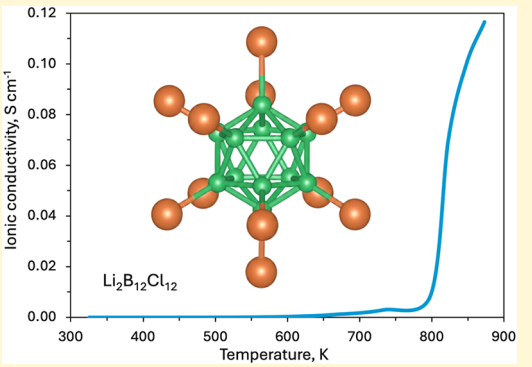
Agnieszka Prus, Hui Wu, Wei Zhou, Austin Bhandarkar, Joseph A. Teprovich Jr, Karol J. Fijalkowski, A. Alec Talin, and Vitalie Stavila*

Cite This: *Chem. Mater.* 2026, 38, 5960−5972

Read Online

ACCESS | Metrics & More | Article Recommendations | Supporting Information

ABSTRACT: Solid electrolytes with suitable conductivity and stability are a key element in overcoming the inherent drawbacks of liquid organic electrolytes in advanced battery systems. This requires comprehensive research into ion transport in various types of solid compounds in order to understand the complex relationships between their composition, structure, and properties. In this paper, we systematically examine the crystal structures and ion transport properties of the perhalogenated lithium *closo*-dodecaborate salts $Li_2B_{12}X_{12}$, where X = F, Cl, Br, and I. The compounds were isolated in anhydrous form and their structures determined by X-ray diffraction over a wide temperature range. Additional characterization was performed using thermal analysis, FTIR, and Raman spectroscopy, while DFT calculations were employed to rationalize the observed trends. $Li_2B_{12}F_{12}$ crystallizes in the *Cmca* space group, while the other salts adopt the $Pn\bar{3}$ symmetry. The $Li_2B_{12}Cl_{12}$ and $Li_2B_{12}Br_{12}$ compounds exhibit polymorphic transformations with transition temperatures around 859 and 865 K, respectively, which are well above that of $Li_2B_{12}H_{12}$. This behavior likely arises from the larger size and greater mass of the perhalogenated anions, which hinder reorientational dynamics at lower temperatures. In contrast, at high-temperatures the disordered phases exhibit high Li^+ ionic conductivity values, reaching 0.12 S cm^{-1} for $Li_2B_{12}Cl_{12}$ and 0.052 S cm^{-1} for $Li_2B_{12}Br_{12}$ (at ≈870 K). Overall, the synergistic blend of structural disorder and inherent thermal and electrochemical stability positions the perhalogenated *closo*-dodecaborates as a robust platform for the development of high-performance electrolytes for various electrochemical devices.

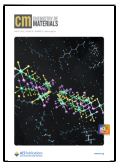


INTRODUCTION

Metal *closo*-polyborates have been intensively studied in recent years as highly promising ionic conductors, often reaching superionic conductivity.[1−5] Their performance is largely due to the presence of large weakly coordinating *closo*-polyborate anions which can undergo rapid reorientations, minimizing cation−anion interactions and boosting ion mobility.[6−8] A characteristic feature of these compounds is the thermally induced phase transition to a disordered structure in which the large weakly coordinating anions rotate freely, dramatically enhancing cation transport in the high-temperature phase.[9] For example, $Ag_2B_{12}H_{12}$ crystallizes at room temperature in the $Pa\bar{3}$ space group with conductivity of about 10^{-5} S cm^{-1}, surging to 3×10^{-3} S cm^{-1} after an entropy-driven phase transition to highly disordered $Fm\bar{3}m$ at 573 K[4]. $Na_2B_{12}H_{12}$ ($P2_1/n$ symmetry) displays a RT conductivity of 8×10^{-7} S cm^{-1},[10] increasing to 0.1 S cm^{-1} near 529 K in the high-temperature form ($Im\bar{3}m$ symmetry)[3,10,11] While $Li_2B_{12}H_{12}$ ($Pa\bar{3}$ symmetry) reaches a higher room temperature ionic conductivity of 10^{-4} S cm^{-1}, it becomes unstable and decomposes after its phase transition at around 625 K, making conductivity measurements difficult.[3,12,13] Recent DFT simulation efforts to understand and predict the conductivity of high-temperature $Li_2B_{12}H_{12}$ showed a conductivity of about 10^{-1} S cm^{-1} at 700 K.[14] This liquid-like conductivity is driven by entropy-mediated phase transitions, and the resulting conductivity enhancement enables fast ion transport while maintaining structural integrity and stability, positioning *closo*-polyborates (and *closo*-polycarborates) as promising solid electrolytes for next-generation batteries.[15−17]

Increasing demand for portable electronic devices, electric vehicles, and grid-scale energy storage is driving the development of next-generation electrochemical energy storage devices.[18] Among these devices, lithium-ion batteries are of particular interest, because of their high gravimetric energy density compared to other systems. Solid electrolytes in lithium-ion batteries are an alternative to the currently widespread liquid electrolytes, because of their superior safety and stability with various electrode materials.[19] However,

Received: January 23, 2026
Revised: May 23, 2026
Accepted: May 27, 2026
Published: June 4, 2026



Downloaded via NATL INST OF STANDARDS & TECHNOLOGY on June 25, 2026 at 19:49:45 (UTC).
See https://pubs.acs.org/sharingguidelines for options on how to legitimately share published articles.

ACS Publications

© 2026 American Chemical Society

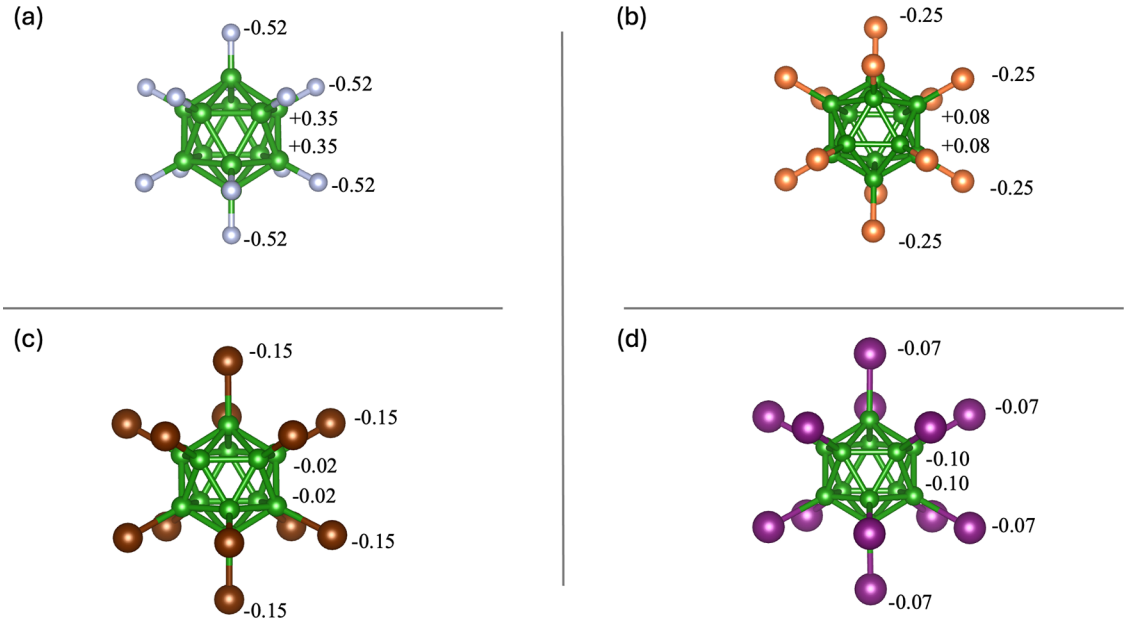


Figure 1. Mulliken charges in the anions of halogenated lithium *closo*-borates (a) $B_{12}F_{12}^{2-}$, (b) $B_{12}Cl_{12}^{2-}$, (c) $B_{12}Br_{12}^{2-}$, (d) $B_{12}I_{12}^{2-}$.

challenges persist with their lower conductivity compared to liquid electrolytes, alongside scale-up and integration hurdles in battery fabrication. The *closo*-borates could also serve as components that provide lithium atoms in polymer gel electrolytes,[15] which display high ionic conductivity, comparable to that of liquid electrolytes.[20] In addition, polymer gel electrolytes are mechanically stable and inhibit the formation of dendrites on the lithium electrode surface, bridging the gap between liquid organic electrolytes and solid electrolytes. Nevertheless, incomplete understanding of the mechanisms governing ionic conductivity in solids and composites continues to hinder the rational design of competitive solid electrolytes.[21]

The expanding group of *closo*-borate conductors can provide essential information about the factors affecting ion transport in solids.[3] Order−disorder phase transitions in *closo*-borates arise from synergistic factors including lattice symmetry, anion polarizability, moment of inertia of the anion, anion reorientation mobility and also asymmetry of the anion.[22,23] Targeted modifications of these parameters can dramatically enhance performance, for instance, substituting one boron atom with carbon in $Li_2B_{12}H_{12}$ lowers the phase transition temperature from over 600 to 400 K, yielding a conductivity value of >0.1 S cm^{-1} for $LiCB_{11}H_{12}$,[24] likely due to favorable 1:1 cation:anion stoichiometry. The study of $Li_2B_{10}H_{10}$ and $LiCB_9H_{10}$ salts supports the thesis that monovalent anions favor a lowering of the *closo*-borate phase transition temperature to a disordered high conductivity form, with $LiCB_9H_{10}$ having a phase transition temperature of about 340 K, which is even lower than that of $LiCB_{11}H_{12}$.[25] For the partially halogenated lithium *closo*-borate derivatives $LiCHB_{11}H_5Cl_6$ and $LiCHB_{11}H_5Br_6$ with much weaker coordination but higher molecular weight, the phase transition occurs at much higher temperatures of 555 and 578 K.[26] The increase in phase transition temperature due to halogenation suggests that the increase in mass is the predominant factor associated with the disordered phase transition for $LiCHB_{11}H_5Cl_6$ and $LiCHB_{11}H_5Br_6$. In the case of the sodium salts, complete halogenation of the *closo*-borates leads to a relatively small change in phase transition temperature relative to the increase in mass, suggesting that the changes in phase transition temperature are in fact the result of a combination of several competing factors. However, the precise impact of borate cluster modifications on phase transition temperature and ionic conductivity remains unclear, hindering the design of new materials and impeding a full understanding of structure−function relationships.

This paper presents a comprehensive synthesis and structural characterization of perhalogenated lithium *closo*-dodecaborates $Li_2B_{12}X_{12}$ (X = F, Cl, Br, I) and investigates their ionic conductivity and thermal/electrochemical stability. Room temperature and high temperature crystalline structures were solved by X-ray diffraction (XRD), showing a rich structural chemistry and a wide thermal stability range. Structural tendencies are discussed and compared with previous studies to further investigate factors influencing polymorphic transitions, such as the size and mass of the anion, the directionality of the anion bond to the lithium atom, and the charge distribution and polarizibility of the B−X bonds (Figure 1). In addition, electrochemical studies were performed, demonstrating high ionic conductivity and robust electrochemical stability for the perhalogenated lithium *closo*-dodecaborates $Li_2B_{12}X_{12}$ (X = F, Cl, Br, I).

EXPERIMENTAL AND THEORETICAL METHODS

Synthesis of Anhydrous $Li_2B_{12}F_{12}$

The hydrated $Li_2B_{12}F_{12}$ salt used in this research was sourced from Boron Specialties, Inc. $Li_2B_{12}F_{12}$ was initially dried for 2 h under vacuum at 110 °C, followed by additional vacuum drying at 200 °C for 2 days (until FTIR spectra showed no H_2O signal at around 3600 cm^{-1}). The purity and anhydrous character of the product were confirmed by XRD (Supporting Information (SI), Figure S10)

Synthesis of Anhydrous $Li_2B_{12}Cl_{12}$

A solution of 2.00 g of sodium dodecachloro-*closo*-dodecaborate ($Na_2B_{12}Cl_{12}$) (Katchem) were passed through an acid-activated Amberlite cation-exchange resin column from Sigma-Aldrich. The acidic fraction was neutralized with LiOH until the pH reached 7, after which all the water was removed using a rotary evaporator. The

https://doi.org/10.1021/acs.chemmater.6c00218
Chem. Mater. 2026, 38, 5960−5972

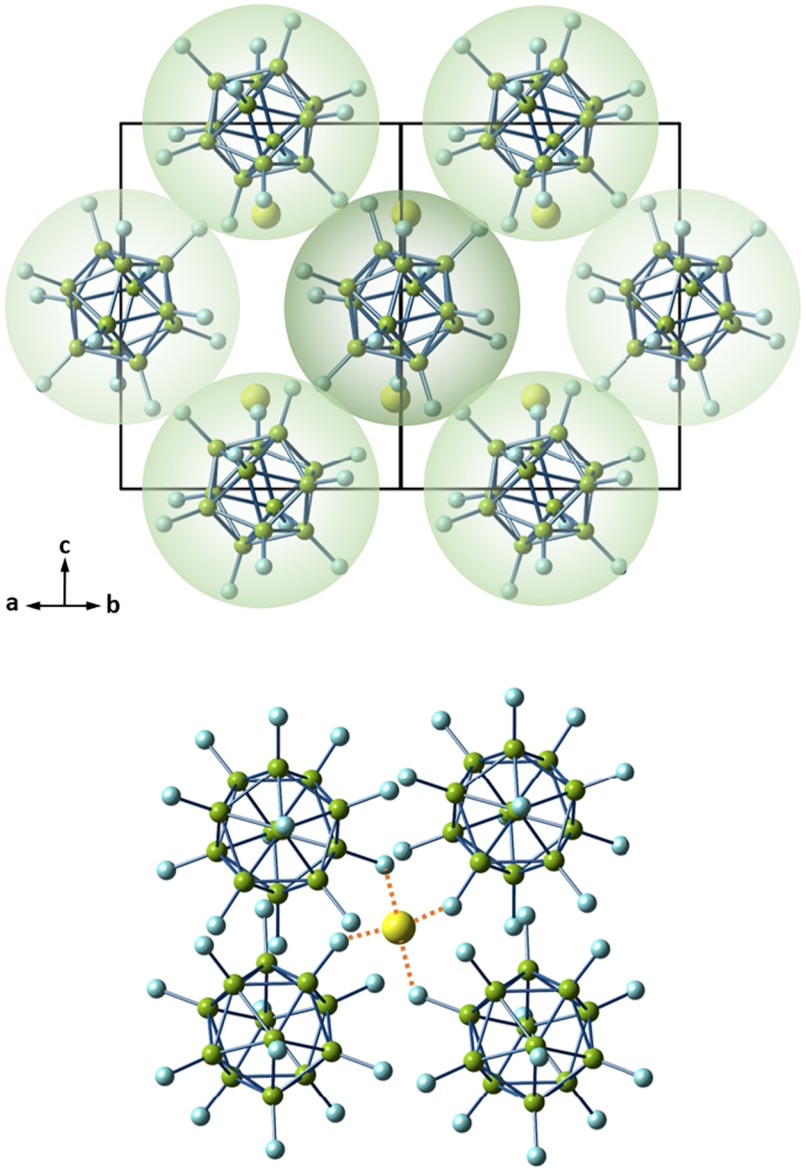


Figure 2. (Top) An (110) view of the crystal structure of $Li_2B_{12}F_{12}$ with the space group *Cmca*. Li^+ cations are located at eight tetrahedral interstitial sites; (bottom) The tetrahedral coordination of Li^+: Each Li^+ is directly coordinated to four F^- from each of the four surrounding $B_{12}F_{12}^{2-}$ anions. Li, B and F are represented by small yellow, green, and cyan solid spheres. The pseudo cubic close packing (CCP) array of $B_{12}F_{12}^{2-}$ anions are illustrated by large transparent green spheres.

resulting powder was then dried by heating under vacuum at 120 °C for 2 h. The powder was then left to stand under vacuum for two more days at 200 °C to ensure it was completely dry. The purity and dryness of the product were confirmed by XRD (SI, Figure S11).

Synthesis of Anhydrous $Li_2B_{12}Br_{12}$

1.00 g of $Cs_2B_{12}H_{12}$ was dissolved in 30 mL of a 1:1 water−methanol mixture. The solution was cooled in an ice bath, and excess liquid bromine was added dropwise. First, 2 mL of Br_2 was added, and the reaction vessel was removed from the ice bath. Another 2 mL of Br_2 was added and the solution was heated to reflux (64−66 °C) for 5 h. After cooling to RT, the solution was evaporated using a rotary evaporator. It was then recrystallized until a pure, homogeneous white powder was obtained. After initial drying in air, the sample was dried at 220 °C under vacuum for 2 h, after which it was left under vacuum for a further 2 days at RT. Characterization via XRD and FTIR confirmed the anhydrous nature and purity of the product (SI, Figure S12)

Synthesis of Anhydrous $Li_2B_{12}I_{12}$

A solution of 1.50 g of $Na_2B_{12}I_{12}$ (Katchem) in water was passed through an acid-activated cation resin column (Sigma-Aldrich). The acid fraction was neutralized with LiOH until the pH reached 7. As the solution was slightly cloudy, it was filtered through a syringe filter. Water was removed using a rotary evaporator and the resulting powder was dried at 200 °C in vacuum for 2 h, followed further drying for 2 days under vacuum at RT. Samples of $Li_2B_{12}I_{12}$ for XRD measurements were prepared by dissolving the sample in acetonitrile and slowly removing the solvent using a rotary evaporator to obtain more crystalline specimens. XRD measurements confirmed the purity and complete dehydration of the resulting powder (SI, Figure S13).

XRD measurements were performed using a Synergy-S Rigaku diffractometer using Cu radiation. Samples were placed in 0.3 mm quartz capillaries and measurements were made over a wide temperature range, from 300 to 960 K, using a hot gas capillary heater. An Agilent Cary-630 ATR-FTIR spectrometer was used to measure the infrared spectra of powder samples, with a module containing a diamond crystal. For Raman spectra measurements,

https://doi.org/10.1021/acs.chemmater.6c00218
Chem. Mater. 2026, 38, 5960−5972

Table 1. Structural Parameters of $Li_2B_{12}X_{12}$ (X = F, Cl, Br, and I) Determined from This Work[a]

Compound	T (K)	Crystal system	Space group	Lattice Parameters			Z	V (Å^3)	V/Z
				a (Å)	b (Å)	c (Å)			
$Li_2B_{12}H_{12}$[30]	293	cubic	$Pa\bar{3}$	9.5771(2)	-	-	4	878.43(6)	219.61
$Li_2B_{12}F_{12}$	298	orthorh.	*Cmca*	12.004(3)	10.308(4)	10.266(2)	4	1270.3(5)	317.58
	475	orthorh.	*Cmca*	11.907(1)	10.455(1)	10.3719(9)	4	1291.1(3)	322.78
$Li_2B_{12}Cl_{12}$	298	cubic	$Pn\bar{3}$	10.0618(6)	-	-	2	1018.7(2)	509.35
	400	cubic	$Pn\bar{3}$	10.1076(3)	-	-	2	1032.62(9)	516.31
	810	cubic	$Fm\bar{3}m$	13.053(1)	-	-	4	2224.4(6)	556.10
$Li_2B_{12}Br_{12}$	500	cubic	$Pn\bar{3}$	10.5834(3)	-	-	2	1185.43(9)	592.72
	700	cubic	$Pn\bar{3}$	10.6547(2)	-	-	2	1209.56(9)	604.78
	800	cubic	$Fm\bar{3}m$	13.647(1)	-	-	4	2541.3(8)	635.33
$Li_2B_{12}I_{12}$	500	cubic	$Pn\bar{3}$	11.2960(3)	-	-	2	1441.4(1)	720.70
$Na_2B_{12}F_{12}$[31]	5	hex.	$P\bar{3}$	12.012(1)	-	7.335(1)	3	916.5(1)	305.50
$Na_2B_{12}Cl_{12}$[31]	295	cubic	$Pa\bar{3}$	12.5577(9)	-	-	4	1980.3(4)	495.08
$Na_2B_{12}Cl12$[2]	838	cubic	$Fm\bar{3}m$	13.216(2)	-	-	4	2308.1(5)	577.03
$Cs_2B_{12}Cl_{12}$	293	trig.	$R\bar{3}$	9.596(7)	-	45.642(2)	6	3641.0(6)	606.8
	473	cubic	$Pm\bar{3}n$	10.519(8)	-	-	2	1164.3(7)	581.2
	293	cubic	$Ia\bar{3}d$	21.022(3)	-	-	16	9299.2(9)	582.2
$Cs_2B_{12}Br_{12}$	293	trig.	$R\bar{3}$	9.979(2)	-	47.664(2)	6	4110.6(3)	685.1
$Cs_2B_{12}I_{12}$	293	trig.	$R\bar{3}$	10.470(5)	-	50.183(3)	6	4765.2(2)	794.2

[a]All results from this work unless otherwise indicated.

samples were prepared in sealed capillaries using a Renishaw Raman Microscope with a 532 nm laser excitation source and ≈50 μW power at the sample. Residual Gas Analysis (RGA) was performed on anhydrous salts using an SRS-300 instrument from Stanford Research Systems, Inc. The anhydrous $Li_2B_{12}X_{12}$ (X = F, Cl, Br, I) powders were loaded inside Swagelok stainless steel sample holders in a nitrogen-filled glovebox, then heated to 298 or 873 K, and small gas aliquots analyzed by RGA.

The crystal structures of $Li_2B_{12}X_{12}$ were first solved using direct space methods based on the lab powder XRD data. Due to the insensitivity of X-ray to the lightweight elements, the first-principles molecular dynamics simulated annealing were subsequently performed to optimize the $B_{12}X_{12}$ configuration and the Li positions with the lowest energy in the initially solved structural models, followed by Rietveld structural refinement (Supporting Information, Figures S1–S9) on the optimal structural model using the GSAS package.[27] Due to the relatively poor X-ray sensitivity to the lightweight elements and the inadequate number of observations of the lab powder XRD data, for $Li_2B_{12}F_{12}$ (which has more independent refinable parameters due to its low symmetry), the $B_{12}F_{12}^{2-}$ was kept as a rigid body with relaxed bond lengths and bond angles in order to maintain the integrity of anion geometry and a stable refinement. The Li–F bond distances were also restrained with the common Li–F distances; for $Li_2B_{12}X_{12}$, X = Cl, Br, and I, with a high cubic symmetry and Li at special Wyckoff site, the atomic positions of B and X were refined with restraints on the B–B, B–X and Li–X bond lengths. The magnitudes of thermal parameters from Rietveld refinement on XRD powder data are notoriously inaccurate. They are listed in the crystallographic information files (CIFs) provided in the Supporting Information (SI), but we do not ascribe any significance to their values.

AC impedance measurements were carried under inert Ar gas. Solid electrolyte powders were pressed into free-standing pellets with a diameter of 10.0 mm and a thickness of 2.9–3.6 mm. The pellets were formed under 100 MPa uniaxial pressure using a Carver hydraulic press and then assembled into an MTI stainless steel cell using mica for electrical insulation and Au electrodes on both sides of the pellet. Measurements were performed over the temperature range from room temperature up to 873 K for all compounds. Sample temperature was monitored with a calibrated thermocouple. Electrochemical impedance spectra were collected from 0.1 Hz to 1 MHz using a Gamry potentiostat operated at 10 or 20 mV AC voltage.

The ionogel was obtained by dissolving poly(vinylidene fluoride) (PVDF) in acetone (76 g/L), both of which were purchased from Sigma-Aldrich. The solution of $Li_2B_{12}X_{12}$ in 1-butyl-1-methylpyrrolidinium *bis*(trifluoromethylsulfonyl)imide (PYR-14-TFSI) was then made. PYR-14-TFSI was purchased from Solvionic. The $Li_2B_{12}X_{12}$ solutions obtained in this way were diluted with propylene carbonate (PC) from Sigma-Aldrich to improve the solubility of the salt to a concentration close to 0.05 M. Those two solutions (ionogel and $Li_2B_{12}X_{12}$ solution) were mixed in a 329:53 ratio and vortexed for 10 s. The ionogel was then used in studies of both the conductivity and electrochemical stability as a gel electrolyte.

First-principles DFT calculations were performed using the Quantum ESPRESSO package.[28] We used Vanderbilt-type ultrasoft pseudopotentials with Perdew–Burke–Ernzerhof exchange correlations. A cutoff energy of 544 eV and appropriately chosen *k*-point meshes were used and found to be enough for the total energies to converge within 0.01 meV/atom. First, all crystal structures were fully optimized with respect to the atomic coordinates. To assist in the interpretation of the IR and Raman data, we further performed density functional perturbation theory (DFPT) calculations[29] and predicted infrared absorption cross sections and Raman intensities. In the DFPT calculations, a larger cutoff energy of 1088 eV and denser *k*-point meshes were used to ensure adequate accuracy.

RESULTS AND DISCUSSION

Structural Investigation of $Li_2B_{12}X_{12}$ Compounds

$Li_2B_{12}F_{12}$. The majority of the diffraction peaks in the room temperature powder XRD pattern of $Li_2B_{12}F_{12}$ can be indexed to an orthorhombic structure with the space group *Cmca* (No.64). The crystal structure was then solved with this symmetry. $Li_2B_{12}F_{12}$ was found to maintain this orthorhombic structure from room temperature up to 850 K. The crystal structure and the Rietveld fit to the XRD patterns at room temperature and at 475 K of $Li_2B_{12}F_{12}$ are shown in Figures 2, S1, and S2. The refined lattice parameters are summarized in Table 1.

As shown in Figure 2, $Li_2B_{12}F_{12}$ possesses an ordered orthorhombic structure with approximately similar *a*, *b*, and *c* lattice parameters. The numbers of anions and cations per unit cell (*i.e.*, four $B_{12}F_{12}^{2-}$ anions and eight Li^+ cations) are the

https://doi.org/10.1021/acs.chemmater.6c00218
Chem. Mater. 2026, 38, 5960–5972

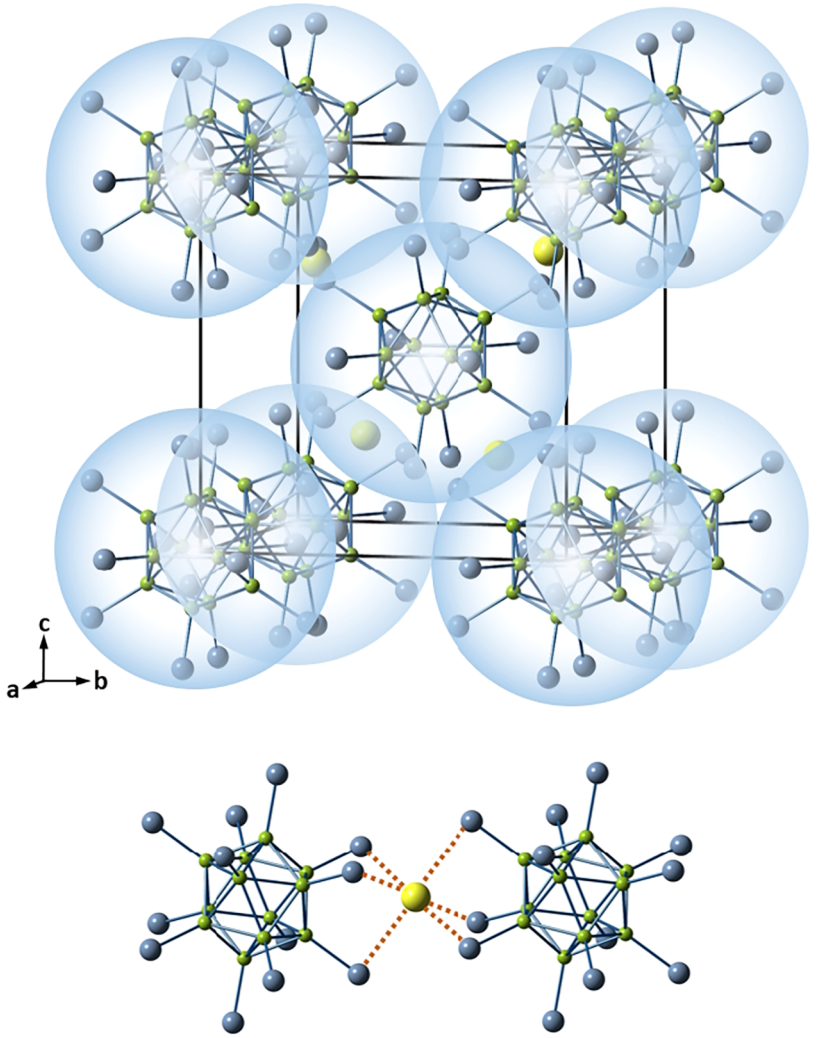


Figure 3. (Top) An off-(100) view of the ordered crystal structure of $Li_2B_{12}Cl_{12}$ with space group $Pn\bar{3}$. Each Li^+ is at the middle point between the two closest adjacent $B_{12}Cl_{12}^{2-}$ anions; (bottom) The local octahedral coordination of Li^+: each Li is directly coordinated to six Cl^- from the two neighboring $B_{12}Cl_{12}^{2-}$ anions. Li, B, and Cl are represented by small yellow, green, and blue solid spheres. The body-centered cubic (BCC) packing of the ordered $B_{12}Cl_{12}^{2-}$ anions are illustrated by large transparent blue spheres.

same as those of its *closo*-hydroborate counterpart $Li_2B_{12}H_{12}$ although the latter forms a cubic structure (space group $Pa\bar{3}$)[30] Similar to the cubic close packing (CCP) of the $B_{12}H_{12}^{2-}$ anion lattice found in $Li_2B_{12}H_{12}$, the $B_{12}F_{12}^{2-}$ anions in the orthorhombic lattice forms a pseudo CCP array in $Li_2B_{12}F_{12}$. Different from $Li_2B_{12}H_{12}$ where Li is at the center of the triangular plane formed by three $B_{12}H_{12}^{2-}$ anions, with increasing size of the $B_{12}F_{12}^{2-}$ anions, in $Li_2B_{12}F_{12}$ each Li is located at the center of the tetrahedral site surrounded by four adjacent $B_{12}F_{12}^{2-}$ anions and directly bonded to four F from each of the neighboring $B_{12}F_{12}^{2-}$ anions, forming a regular LiF_4 tetrahedron with Li−F distances of 1.90 Å−1.91 Å due to its larger size relative to $B_{12}H_{12}^{2-}$. In addition, due to the different sizes of anions, one $B_{12}F_{12}^{2-}$ anion is surrounded by eight Li^+ cations in $Li_2B_{12}F_{12}$, whereas only six Li^+ cations are needed to encompass one $B_{12}H_{12}^{2-}$ anion in $Li_2B_{12}H_{12}$. On the other hand, if keeping the same halogenated *closo*-dodecaborate anion $B_{12}F_{12}^{2-}$ while increasing the alkali cation size from Li^+ to Na^+, the resultant $Na_2B_{12}F_{12}$ was found to form a hexagonal structure (space group $P\bar{3}$) with a pseudo body-centered cubic (BCC) array of anion packing motif, and the larger size Na^+ cation is coordinated to six F in a regular NaF_6 trigonal prism.[31]

$Li_2B_{12}Cl_{12}$. When the halogen atom changes from F to Cl, the room temperature powder XRD patterns of $Li_2B_{12}Cl_{12}$ exhibit a drastic change compared to that of $Li_2B_{12}F_{12}$ (Figure S3). These diffraction peaks can be indexed into a cubic structure with the space group $Pn\bar{3}$ (No. 201). From our temperature-controlled XRD experiments, the XRD patterns of $Li_2B_{12}Cl_{12}$ were found to remain the same from room temperature up to 700 K except some small peak shifting due to thermal expansion. A new set of peaks starts to emerge beyond 750 K, coexisting with those of the low-temperature $Pn\bar{3}$ structure up until 800 K. At 810 K, the diffraction peaks from the low-temperature phase completely disappear, and only the peaks of the high-temperature phase remain with a diffuse scattering background. These new high-temperature peaks can be indexed into a cubic structure with the space group $Fm\bar{3}m$ (No. 225). Both the "low temperature" $Pn\bar{3}$ and the "high temperature" $Fm\bar{3}m$ structures of $Li_2B_{12}Cl_{12}$ were determined and refined, and the Rietveld fits to the XRD patterns of $Li_2B_{12}Cl_{12}$ at various temperatures are shown in

https://doi.org/10.1021/acs.chemmater.6c00218
Chem. Mater. 2026, 38, 5960−5972

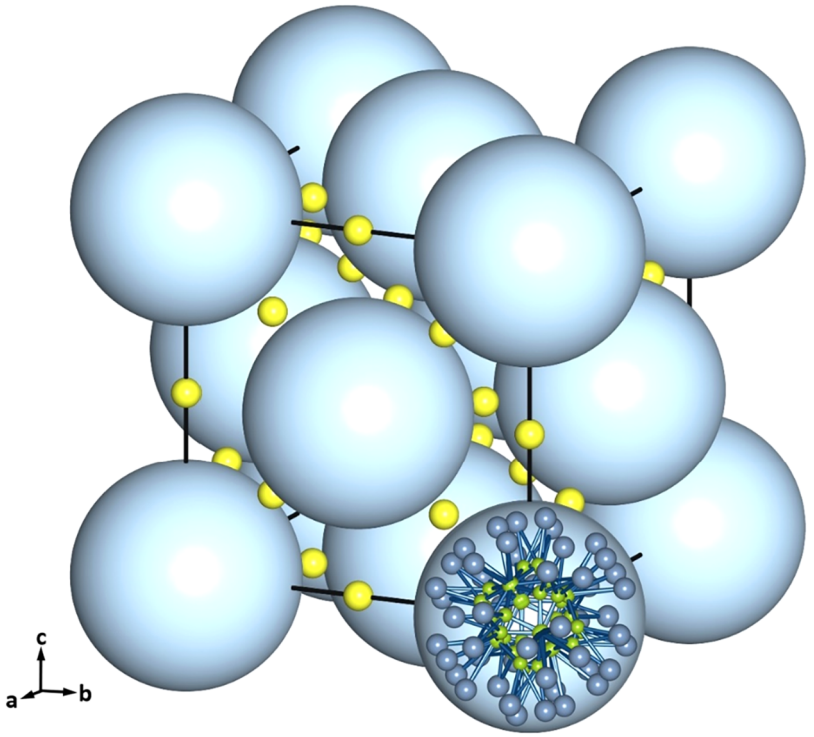


Figure 4. Disordered high-temperature structure (space group $Fm\bar{3}m$) of $Li_2B_{12}Cl_{12}$. The face-centered cubic (FCC) packing of the disordered $B_{12}Cl_{12}^{2-}$ anions are illustrated by large light blue spheres. For clarity, only one disorderly oriented $B_{12}Cl_{12}^{2-}$ anion is superimposed to aid the reader. Li, B and Cl are represented by small yellow, green, and blue solid spheres.

Figures S3−S5, and the corresponding refined lattice parameters are listed in Table 1.

As shown in Figure 3, the room temperature ordered structure of $Li_2B_{12}Cl_{12}$ exhibits a body-centered cubic (BCC) array of the ordered $B_{12}Cl_{12}^{2-}$ anions. With increasing $B_{12}X_{12}^{2-}$ anion size from F to Cl, the small Li^+ was found to be at the middle point between the two closest $B_{12}Cl_{12}^{2-}$ anions, i.e. the two $B_{12}Cl_{12}^{2-}$ anions at the body-center and at the corner of a cubic cell. Each Li^+ is directly coordinated to six Cl^- from the two neighboring $B_{12}Cl_{12}^{2-}$ anions with Li−Cl distances of 2.64 Å (×6), forming a regular $LiCl_6$ octahedron. Theoretically, in a BCC unit cell, there should be eight such equivalent cation sites in a close contact with a $B_{12}Cl_{12}^{2-}$ anion, i.e., each $B_{12}Cl_{12}^{2-}$ anion is surrounded by eight Li^+ cation sites. However, there are only two $B_{12}Cl_{12}^{2-}$ anions within one unit cell. Hence, only four Li^+ cations should be allowed in a unit cell to maintain the overall charge neutrality. Assessment of the diffraction extinction of the observed XRD patterns indicates the most probable space group to be $Pn\bar{3}$. Under this symmetry there would be two crystallographically independent sites with a multiplicity of 4 for each site (*i.e.*, 4*b* and 4*c* Wyckoff sites). If only four of these eight possible sites are fully occupied by Li, $Li_2B_{12}Cl_{12}$ will form a cation-ordered structure (*e.g.*, Figure 3 shows that only the 4*b* site is occupied). On the other hand, if Li^+ cations populates all eight equivalent sites with a partial occupancy, the delocalization of cations will result in a "cation-disordered" structure and increase the symmetry to the space group $Im\bar{3}$. In such a structure, $B_{12}Cl_{12}^-$ anions remain the same BCC arrangement while Li^+ cations will be at the 8*c* Wyckoff site under the $Im\bar{3}$ symmetry. However, the appearance of the (111) peak in the present XRD patterns below 750 K violates the "I" symmetry reflection conditions. Therefore, the low-temperature phase of $Li_2B_{12}Cl_{12}$ should be the $Pn\bar{3}$ structure with ordering of both cations and anions based on the diffraction results.

The ordered $Pn\bar{3}$ structure with a BCC lattice of $Li_2B_{12}Cl_{12}$ is distinct from the ordered structure of $Na_2B_{12}Cl_{12}$ with the $Pa\bar{3}$ symmetry.[31] The latter is isostructural to many other metal-*closo*-dodecaborates such as $Li_2B_{12}H_{12}$[30] and $Ag_2B_{12}Cl_{12}$[32] with a CCP or face-centered cubic (FCC) lattice of anions. Apparently, the BCC array of $B_{12}Cl_{12}^{2-}$ anions in $Li_2B_{12}Cl_{12}$ is less efficiently packed than the FCC arrays in $Na_2B_{12}Cl_{12}$, as indicated by the larger volume per formula unit (V/Z) of $Li_2B_{12}Cl_{12}$ than that of $Na_2B_{12}Cl_{12}$ (Table 1). In addition, different from the Li^+ cation coordination sphere in the BCC lattice (Figure 3), in $Na_2B_{12}Cl_{12}$ each Na^+ cation is at the center of a triangular plane defined by three surrounding $B_{12}Cl_{12}^-$ anions and coordinated to six Cl from these $B_{12}Cl_{12}^-$ anions, resulting in a distorted $NaCl_6$ octahedron[31]

The high-temperature phase of $Li_2B_{12}Cl_{12}$ at 810 K transforms into a completely disordered $Fm\bar{3}m$ structure as a result of the almost isotropic reorientational disordering of the anions on the diffraction time scale (Figure 4), and is similar to other face-centered cubic (FCC) structure of the high-temperature phase of the metal *nido*- and *closo*-(carba)-borates[11,25,33,34] and halogenated sodium-*closo*-dodecaborates.[2] Determination of Li position is challenging due to the disordering in both cation sites and anion reorientation, the limited number of diffraction peaks from high symmetry, as well as the insensitivity of X-rays to the lightweight Li. In the present study, Li^+ cations were assigned at the 4*b* and 24*d* Wyckoff sites under the $Fm\bar{3}m$ space group with partial occupancies similar to those in the high temperature phase of $Na_2B_{12}Cl_{12}$.[2]

$Li_2B_{12}Br_{12}$. From our temperature-controlled XRD studies, $Li_2B_{12}Br_{12}$ is found to crystallize in the cubic $Pn\bar{3}$ symmetry

https://doi.org/10.1021/acs.chemmater.6c00218
Chem. Mater. 2026, 38, 5960−5972

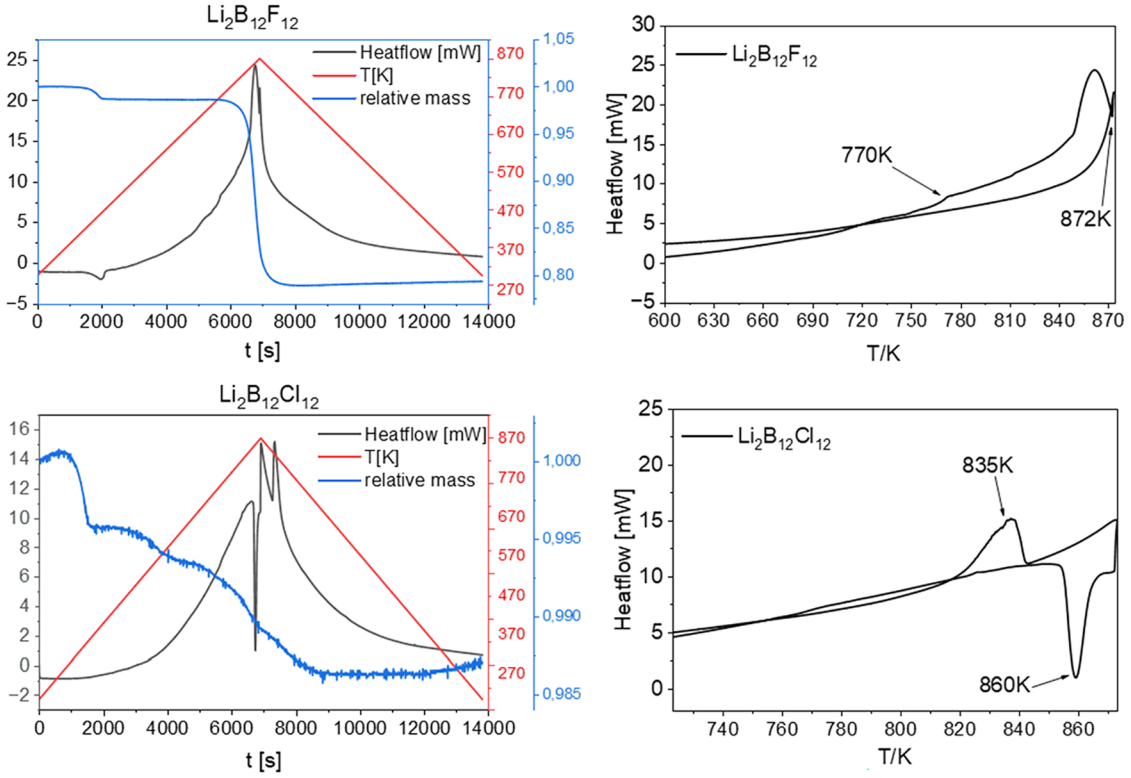


Figure 5. Combined thermogravimetric analysis (TGA) and differential scanning calorimetry (DSC) of $Li_2B_{12}F_{12}$ (top) and $Li_2B_{12}Cl_{12}$ (down).

and is isostructural to $Li_2B_{12}Cl_{12}$ in the studied temperature range up to 780 K. At temperatures ≥790 K, the ordered phase of $Li_2B_{12}Br_{12}$ undergoes a similar order−disorder polymorphic phase transition to the completely disordered $Fm\bar{3}m$ structure as $Li_2B_{12}Cl_{12}$. It is difficult to obtain high-quality XRD patterns from the anhydrous sample at RT, as the removal of the solvent tends to yield low-crystallinity samples. Nonetheless, the Rietveld fit of XRD patterns of the ordered and disordered structures of the anhydrous $Li_2B_{12}Br_{12}$ at high temperatures are shown in Figures S6−S8 (SI).

$Li_2B_{12}I_{12}$. A well crystalline anhydrous $Li_2B_{12}I_{12}$ sample is difficult to obtain at room temperature. The XRD pattern of a dry $Li_2B_{12}I_{12}$ sample at 500 K with an elevated background indicates the formation of a same $Pn\bar{3}$ structure as its Cl and Br analogues (Figure S9, SI). The XRD patterns remain nearly unchanged up to 810 K except the slight peak shift and increased background with temperature. $Li_2B_{12}I_{12}$ starts to decompose upon further heating from 810 to 960 K. Some residual peaks from the $Pn\bar{3}$ phase still can be observed at 960 K, while the prominent background prevents the identification of any small peaks from the disordered high-temperature phase in this high temperature range.

In contrast, halogenated cesium *closo*-borates, $Cs_2B_{12}Cl_{12}$, where X = Cl, Br, I, unlike the salts analyzed above, crystallize in the trigonal system in the $R\bar{3}$ space group at room temperature, with six molecules of the compound per unit cell. In the low-temperature forms of cesium halogenated *closo*-borates, there are two types of cesium cations: cations coordinated by three $B_{12}X_{12}^{2-}$ anions, with each anion coordinating the cesium cation via three halogen atoms, and cations coordinated tetrahedrally by four $B_{12}X_{12}^{2-}$ anions, each via three halogen atoms. This structure contains two types of $B_{12}X_{12}^{2-}$ anion, which differ significantly in terms of their cationic environment. In one type, the boron atoms form a cluster-like structure surrounded by six Cs^+ cations arranged in the shape of a distorted octahedron. In another, boron atoms form a type of cluster surrounded by eight Cs^+ cations in the form of a distorted cubic structure.[35]

In the case of $Cs_2B_{12}Cl_{12}$, a phase transition occurs at 471 K to a disordered high-temperature form that crystallizes in the cubic system ($Pm\bar{3}n$ space group), which is directly linked to the transition from a distorted CCP lattice to a primitive P-type lattice. In the high-temperature phase of $Cs_2B_{12}Cl_{12}$, the cesium cation is tetrahedrally coordinated by four anions, each of which is coordinated by three halogen atoms, resulting in a cuboctahedral coordination sphere containing 12 halogen atoms. It has also been observed that upon cooling of the high-temperature form of $Cs_2B_{12}Cl_{12}$ (space group $Pm\bar{3}n$)−a partially ordered, cubic phase with space group $Ia\bar{3}d$ forms, containing as many as 16 units in the unit cell, which is associated with a transition from a P-type cubic lattice to an I-type cubic lattice and a doubling of the lattice constant while retaining the same point group $m3m$, This point group is also seen in the high-temperature phases of $Li_2B_{12}Cl_{12}$, $Na_2B_{12}Cl_{12}$, and $Li_2B_{12}Br_{12}$ (Table 1). The phase transition temperatures of $Cs_2B_{12}Cl_{12}$ to $Cs_2B_{12I}I_{12}$ to the high-temperature phase[36] have been determined to be 625 and 543 K, respectively. All perhalogenated Cs-salts are exceptionally thermally stable, and the decomposition temperatures decrease from $Cs_2B_{12}Cl_{12}$ to $Cs_2B_{12}Br_{12}$ to $Cs_2B_{12I}I_{12}$, reaching 1256, 1232, and 1218 K respectively.

For the $Li_2B_{12}X_{12}$ (X = H, F, Cl, Br and I) series, with halogenation, the anion arrays first exhibit drastic variation from the CCP ($Li_2B_{12}H_{12}$) to a pseudo-CCP ($Li_2B_{12}F_{12}$) and to a BCC ($Li_2B_{12}X_{12}$, X = Cl, Br, and I) lattice; the small Li^+ cations also accommodate themselves with surrounding anions of increasing size, from coordinating to three $B_{12}H_{12}^{2-}$ anions, forming distorted LiH_6 octahedra, to coordinating to four

https://doi.org/10.1021/acs.chemmater.6c00218
Chem. Mater. 2026, 38, 5960−5972

$B_{12}F_{12}^{2-}$ forming LiF_4 tetrahedra, finally to two large $B_{12}X_{12}^{2-}$ (X = Cl, Br, and I) forming regular LiX_6 octahedra. Besides the sizes of cation and anions, other factors may also play roles in affecting such structural variation. Our calculations on Mulliken charges of the halogenated lithium *closo*-dodecaborates indicate that the charged halogen tip of the isolated $[B_{12}X_{12}]^{2-}$ anions becomes less negative from F to I (Figure 1), which will lead to a weaker interaction with surrounding cations from $B_{12}F_{12}^{2-}$ to $B_{12}I_{12}^{2-}$ anions. This is in accord with the previous study in $Na_2B_{12}X_{12}$ (X = H, F and Cl), where the $B_{12}Cl_{12}^{2-}$ was found to have a much weaker relative coordination strength than $B_{12}H_{12}^{2-}$ and $B_{12}F_{12}^{2-}$.[31] The different relative coordination strength of $B_{12}X_{12}^{2-}$ anions in $Na_2B_{12}X_{12}$ also aligns with our experimental observations in $Li_2B_{12}X_{12}$ that from F to I, *i.e.*, $Li_2B_{12}X_{12}$ samples are increasingly prone to form hydrate phases, and the resulting hydrates with larger halogenated anions are more difficult to be dehydrated. The less negative tip of $[B_{12}X_{12}]^{2-}$ anion and the consequently weaker coordination strength with increasing halogen atom size is also seemingly consistent with the smaller number of the Li^+ cations surrounding a $B_{12}Cl_{12}^{2-}$ anion (*i.e.*, four, see Figure 3) than that around a $B_{12}H_{12}^{2-}$ (*i.e.*, six[30]) or a $B_{12}F_{12}^{2-}$ (*i.e.*, eight, see Figure 2) anion.

The calculated electrostatic potential surface maps on $[B_{12}X_{12}]^{2-}$ anions in halogenated sodium-*closo*-dodecaborates[2] indicated an increased anisotropy of charge density distribution around the $B_{12}X_{12}^{2-}$ anions (X = Cl, Br and I) with increasing halogen atom size even though the overall charge of these anions remains constant. As a result, the directional charge distribution on the halogen atoms in the $B_{12}X_{12}^{2-}$ anions may lead to strong directional bonds to cation and increase the resistance to reorientational anion disorder. The smaller Li^+ cation with a stronger polarizing power than Na^+ would further enhance such directional bonds between cations and anions, stabilize the ordered structure, and drive the order−disorder phase transition to high temperature. This effect is especially manifest for larger halogen atom with a greater polarizability. Therefore, we observed higher order−disorder phase transition temperatures in $Li_2B_{12}X_{12}$ (X = Cl, Br, and I) than those in their Na analogues, as well as the increased polymorphic phase transition temperatures from Cl to I within the $Li_2B_{12}X_{12}$ series even though the ordered phase of $Li_2B_{12}X_{12}$ (X = Cl, Br, and I) are isostructural. Certainly, the increased mass of heavier halogenated $B_{12}X_{12}^{2-}$ anions may also impose greater energy barrier to their dynamic motion, and thus further elevate the phase transition temperatures. The high-temperature structure of $Li_2B_{12}Cl_{12}$ and $Li_2B_{12}Br_{12}$ exhibit features of partial cation occupancy (cation disordering) and reorientational anion dynamics (anion disordering), which is a signature of "liquid-like" superionic conduction as observed in other Li^+ and Na^+ *closo*-borates.[24,25,33,34]

Thermal Analysis

Figure 5 shows the results of DSC and TGA measurements for $Li_2B_{12}F_{12}$. At 872 K, a sharp downward directed peak is seen in the heating cycle, indicating a thermic transformation. In the cooling cycle, neither an exothermic nor an endothermic process is observed. Above 768 K, there is a decrease in mass of up to 20%, indicating the beginning of decomposition of the compound. The above observations indicate that the onset of thermal decomposition occurs at a temperature lower than any order−disorder phase transition. This is similar to the behavior of $Cs_2B_{12}Cl_{12}$, where a slow mass loss begins at 873 K, and significant decomposition does not occur until temperatures exceed 1250 K.[35] The endothermic event at 872 K likely corresponds to a polymorphic phase transition that occurs as the compound begins to decompose. These results are consistent with the XRD measurements, in which a decrease in peak intensity is observed as the temperature is increased to 850 K (SI, Figure S14). Residual Gas Analysis (RGA) at low temperatures shows no clear signal associated with decomposition. At 873 K, small spectral features at m/z = 19−20, attributed to HF, were observed, confirming that some cage decomposition occurs at high temperatures (SI, Figure S30).

In the case of $Li_2B_{12}Cl_{12}$, an endothermic phase transition was observed in the heating cycle with a peak maximum at 859 K, corresponding to a $Pn\bar{3} \rightarrow Fm\bar{3}m$ phase transition, and an exothermic phase transition was observed at 837 K in the cooling cycle, corresponding to a phase transition from $Fm\bar{3}m$ to $Pn\bar{3}$, which correlates with the XRD measurements (SI, Figure S15). This behavior is analogous to that of the isostructural salt $Na_2B_{12}Cl_{12}$, whose transition to the high-temperature form is at 748 K and is also endothermic, while the transition back to the $Pn\bar{3}$ form occurs at 688 K. In the case of $Li_2B_{12}Cl_{12}$, the area underneath the peak that illustrates the endothermic transition is slightly larger than the area underneath the exothermic peak, suggesting that not all of the high-temperature phase reverts to the low-temperature polymorph, correlating with a slight decrease in mass of about 1%.

For $Li_2B_{12}Br_{12}$, the phase transition from the room-temperature (RT) phase to the high-temperature (HT) phase is not characterized by a well-defined, sharp endothermic peak over the investigated temperature range (SI, Figures S26 and S27). As with $Na_2B_{12}Br_{12}$,[2] the phase transition of $Li_2B_{12}Br_{12}$ is more continuous, even if the rate of temperature change is slow (5 K min^{-1}), and it starts at 842 K and lasts until at least 873 K. Unlike $Na_2B_{12}Br_{12}$, no clear minimum was observed at a particular temperature. At 813 K, the sample's mass begins to decrease slightly (by 1% up to 873 K), indicating the onset of $Li_2B_{12}Br_{12}$ decomposition. In other words, the transition to the HT phase and the slow decomposition of the compound occur in the same temperature range. However, a diffraction pattern from the high-temperature phase was recorded during very slow heating (SI, Figure S16), confirming the phase transition occurs within the temperature range of 842−873 K.

Unlike the chloro- and bromo- analogs, $Li_2B_{12}I_{12}$ shows no discernible phase transition up to 873 K, whereas above 848 K a gradual mass loss accompanied by a broad endothermic signal indicates the onset of thermal decomposition (SI, Figures S28 and S29). These observations suggest that, similar to the halogenated sodium salts of $Na_2B_{12}X_{12}$ (X = Cl, Br, I),[2] the phase transition temperature of the halogenated lithium *closo*-borates increases down the halogen group. However, lithium salts have higher phase transition temperatures than halogenated sodium salts, which may be due to the more directional cation-halogenated anion bond, a consequence of the smaller ionic radius and higher charge density of the lithium cation, which strengthen the cation−anion interactions. In the case of Cs salts, which adopt a different structure, the dominant factor appears to be strong interatomic coordination, manifested in higher coordination numbers, rather than the directionality of the bonds. Hence, although the cesium cation is larger and its bonds are less directional, the thermal stability of cesium salts is higher, exceeding 1200

https://doi.org/10.1021/acs.chemmater.6c00218
Chem. Mater. 2026, 38, 5960−5972

Table 2. FTIR and Raman Active Modes of $Li_2B_{12}X_{12}$ (X = F, Cl, Br, and I)

FTIR	$Li_2B_{12}F_{12}$		$Li_2B_{12}Cl_{12}$		$Li_2B_{12}Br_{12}$		$Li_2B_{12}I_{12}$	
Vibrations	Calc.	exp.	Calc.	exp.	Calc.	exp.	Calc.	exp.
T_u	526	503	220	-	207	-	200	-
T_u	737	721	540	537	447	445	240	-
T_u	1277	1221	1000	986	992	983	944	941
RAMAN	$Li_2B_{12}F_{12}$		$Li_2B_{12}Cl_{12}$		$Li_2B_{12}Br_{12}$		$Li_2B_{12}I_{12}$	
Vibrations	Calc.	exp.	Calc.	exp.	Calc.	exp.	Calc.	exp.
Hg	350	383	150	127	90	82	86	-
Ag	465	430	543	301	193	191	146	147
Hg	398	393	615	-	690	-	142	-
Hg	524	-	797	-	949	-	672	-
Hg	1229	-	954	-	952	-	910	-
Ag	1348	-	997	-	809	-	932	-

K.[35] Furthermore, the lack of transition to the high-temperature phase for $Li_2B_{12}F_{12}$ and $Li_2B_{12}I_{12}$ is also confirmed by *in situ* XRD measurements (SI, Figures S14 and S17−S21). As the temperature increases to 850 and 960 K, respectively, the XRD reflections gradually weaken, indicating significant structural disorder upon heating. RGA measurements on $Li_2B_{12}Cl_{12}$ (SI, Figure S31), $Li_2B_{12}Br_{12}$ (SI, Figure S32), and $Li_2B_{12}I_{12}$ (SI, Figure S33) do not reveal detectable gaseous decomposition products upon heating to 873 K.

Spectroscopic Characterization

In general, the halogenated anions $B_{12}X_{12}^{2-}$ belong to the point group with the highest symmetry (I_h).[2,37,38] The normal vibrations of this group are classified into 2Ag + F1g + 2Gg + 4Hg + 3F1u + 2F2u + 2Gu + 2Hu. Among which only three F1u vibrations are active in IR, two Ag and four Hg vibrations are active in Raman. The calculations and experimental values of the wavelengths and signal intensities of the vibrations from $Li_2B_{12}X_{12}$ (X = F, Cl, Br, I) in FTIR and Raman spectroscopy are shown in Table 2. Experimental spectra and calculated spectra are presented in Supporting Information (Figures S22−S25). The strongest signals in the FTIR and Raman spectra are visible in the experimental spectra of the powder samples and correspond to the wavelength values of the strongest signals in the calculated spectra, confirming that halogenated *closo*-borates were obtained.

Ionic Conductivity

The ionic conductivity of $Li_2B_{12}X_{12}$ (X = F, Cl, Br, I) is shown in Figure 6, and the values were determined from AC impedance measurements on pelletized samples. The halogenated lithium *closo*-dodecaborates possess markedly lower ionic conductivity than their hydrogen analogue $Li_2B_{12}H_{12}$ at ambient temperature, yet their conductivity increases steadily upon heating and for $Li_2B_{12}Cl_{12}$ and $Li_2B_{12}I_{12}$ it rises sharply near the polymorphic phase transition, paralleling the behavior of perhalogenated sodium salts.[2] Below the phase transitions, the conductivities follow the order $Li_2B_{12}Cl_{12}$ > $Li_2B_{12}F_{12}$ > $Li_2B_{12}Br_{12}$ > $Li_2B_{12}I_{12}$ with activation energies ranging from 0.57 eV for $Li_2B_{12}Cl_{12}$ to 0.69 eV for $Li_2B_{12}I_{12}$, and similar to that of $Li_2B_{12}H_{12}$.[2,39] Above the polymorphic phase transition, $Li_2B_{12}Cl_{12}$ and $Li_2B_{12}Br_{12}$ show excellent high-temperature Li^+ conductivities of 0.120 and 0.052 S cm^{-1}, respectively, which is attributed to structural reorientations and increased Li^+ mobility. While the conductivity of $Li_2B_{12}H_{12}$ reaches 2.9 × 10^{-4} S cm^{-1} at 303 K in its pristine form[2] and can be enhanced to 1.2 × 10^{-3} S cm^{-1} at 333 K through ZrO_2 nanocomposite

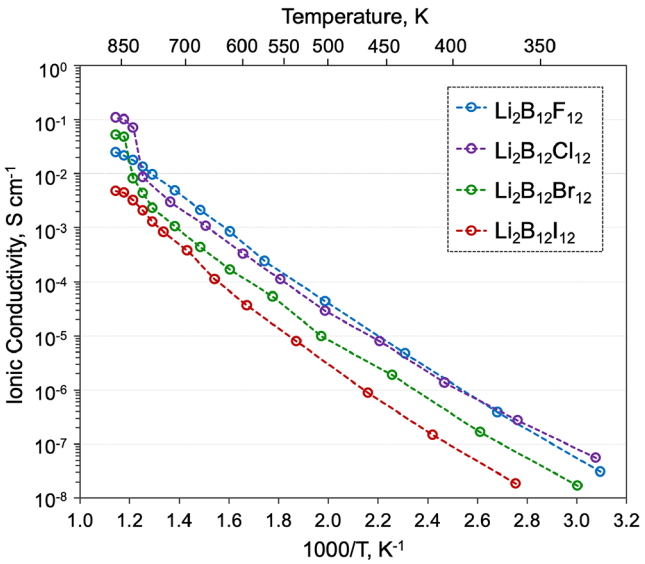


Figure 6. Ionic conductivity of $Li_2B_{12}X_{12}$ compounds (X = F, Cl, Br, I) function of temperature.

formation (which also lowers its activation energy from 0.52 to 0.42 eV),[39] the halogenated Li analogues, despite lower room-temperature performance, achieve high conductivities at elevated temperatures, with $Li_2B_{12}Cl_{12}$ becoming superionic above 820 K. These conductivity values suggest potential utility for the $Li_2B_{12}X_{12}$ compounds as high-temperature solid-state Li^+ conductors, consistent with broader trends in *closo*-polyborate electrolytes.[40−42]

Electrochemical Stability

Defining the electrochemical stability window is a critical prerequisite for the integration of *closo*-borates into energy storage devices, as these limits dictate the safe operational voltage and long-term viability of the cell. Figure 7 shows chronovoltammetry curves recorded in a cell with the configuration stainless steel electrode|$Li_2B_{12}X_{12}$ electrolyte| stainless steel electrode. As indicated by the CV curves, the $Li_2B_{12}F_{12}$ system appears stable up to about 3.0 V, and the addition of the ionic liquid PYR-14-TFSI has only a minor effect on the available potential range (green and blue curves). In the case of $Li_2B_{12}Cl_{12}$, the electrochemical stability is significantly lower, with the potential window narrowed to 2.3 V. In the case of subsequent perhalogenated lithium *closo*-dodecaborates, the electrochemical stability is even weaker; in

https://doi.org/10.1021/acs.chemmater.6c00218
Chem. Mater. 2026, 38, 5960−5972

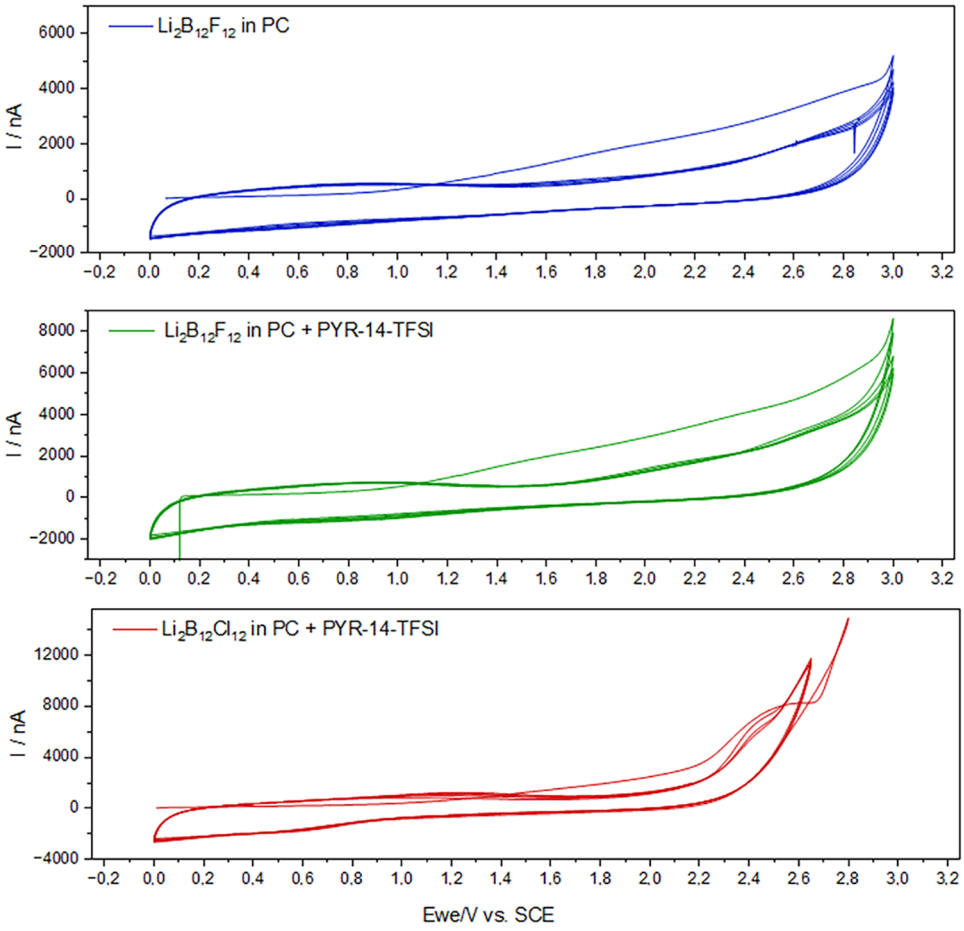


Figure 7. Chronovoltammetry curves of $Li_2B_{12}F_{12}$ and $Li_2B_{12}Cl_{12}$ in polymer gel with PVDF at scan rate 10 mV/s.

other words, the electrochemical stability decreases down the group. Surprisingly, we observed a rather low solubility of the investigated compounds in PYR-14-TFSI, despite the ionic character of *closo*-borate compounds. Impedance studies show that the conductivity at room temperature in the described systems is of the order of 10^{-4} S cm^{-1}, which is consistent with the values previously reported for $Li_2B_{12}H_{12}$ in polymer-gel systems.[43]

These results extend the rapidly growing body of research on solid electrolytes based on Polyboron clusters by demonstrating that fully perhalogenated lithium *closo*-dodecaborates combine the high temperature superionic behavior well documented in $Li_2B_{12}H_{12}$, $Na_2B_{12}H_{12}$, and mixed *closo*-carbahydroborates such as $LiCB_{11}H_{12}$ and $LiCB_9H_{10}$ with markedly enhanced thermal and electrochemical stability.[44] Whereas prior investigations have primarily emphasized hydride clusters, mixed-anion strategies (*e.g.*, $Li_2(CB_{11}H_{12})_x(CB_9H_{10})_{1-x}$), or nanoconfined phases to suppress phase transitions and boost room temperature conductivity, the present findings reveal that systematic perhalogenation coupled with the choice of smaller, more polarizing Li^+ over Na^+ offers an orthogonal design parameter to modulate order−disorder phase transitions, anion reorientational barriers, and Li^+ transport pathways.[9] Notably, the superionic conductivities achieved by $Li_2B_{12}Cl_{12}$ (≈0.12 S cm^{-1}) and $Li_2B_{12}Br_{12}$ (≈0.05 S cm^{-1}) above their order−disorder phase transitions rival those of benchmark complex hydrides, while the wide electrochemical windows echo the stability of recently reported functionalized *closo*-borates and *nido*-borates.[44] By elucidating how anion mass, size, polarizability, and charge anisotropy govern these properties, this study positions the $Li_2B_{12}X_{12}$ series (X = F, Cl, Br, I) as a suitable model system for elucidating structure−property relationships in polyborate electrolyte materials.

CONCLUSIONS

The $Li_2B_{12}X_{12}$ salts (X = F, Cl, Br or I) are thermally robust materials exhibiting high stability over a wide temperature range, exceeding that of $Li_2B_{12}H_{12}$. At room temperature, $Li_2B_{12}F_{12}$ crystallizes in an orthorhombic structure with the space group *Cmca*, while the chloro-, bromo-, and iodo-derivatives adopt a cubic $Pn\bar{3}$ structure. The low-temperature phases of the $Li_2B_{12}X_{12}$ salts (X = Cl, Br) are stable in a wider temperature range, as evidenced by the higher phase transition temperatures, which are approximately 100 °C above those of their sodium counterparts.[2] The elevated transition temperatures reflect stronger and more directional cation−anion bonding in the lithium salts, arising from the smaller ionic radius and stronger polarizing power of Li^+. Above the phase transition temperature, $Li_2B_{12}Cl_{12}$ and $Li_2B_{12}Br_{12}$ form a disordered cubic structure with the $Fm\bar{3}m$ symmetry and exhibit superionic conductivity. No disordered high-temperature phase was observed in $Li_2B_{12}F_{12}$ and $Li_2B_{12}I_{12}$ before decomposition, although their ordered phases are thermally stable up to about 768 and 837 K, respectively. Within the $Li_2B_{12}X_{12}$ series, the charged tips of the $[B_{12}X_{12}]^{2-}$ anion become less negative from F to I, leading to a weaker

https://doi.org/10.1021/acs.chemmater.6c00218
Chem. Mater. 2026, 38, 5960−5972

coordination of $[B_{12}Cl_{12}]^{2-}$ than $[B_{12}F_{12}]^{2-}$ to metal ions as evidenced by the smaller number of the surrounding Li^+ cations around the anions and lower phase transition temperature in $Li_2B_{12}Cl_{12}$ than in $Li_2B_{12}F_{12}$, and more tendency for hydration down the halogen group. On the other hand, for the isostructural $Li_2B_{12}X_{12}$ (X = Cl, Br, and I), from Cl to I, the increased anisotropic charge distribution in the $B_{12}X_{12}$ anion leads to stronger directional bonds to cations and thus greater resistance to reorientational anion disorder,[2] supporting the idea that the reorientation becomes progressively more difficult for heavier and larger anions as evidenced by the increased phase transition temperature from $Li_2B_{12}Cl_{12}$ to $Li_2B_{12}Br_{12}$ and decreased ionic conductivity from $Li_2B_{12}Cl_{12}$ to $Li_2B_{12}I_{12}$.

The combination of exceptional thermal stability and superionic behavior above the phase transition temperature positions $Li_2B_{12}Br_{12}$ and $Li_2B_{12}Cl_{12}$ as promising candidates for thermal batteries. Compositional modifications of pure compounds can further lower polymorphic transition temperatures, extending the application range of these materials, as demonstrated for mixed-anion compounds $Li(CB_9H_{10})_{0.7}(CB_{11}H_{12})_{0.3}$ or $Na_2(CB_9H_{10})(CB_{11}H_{12})$.[45−47] Such modifications may also help stabilize high-temperature forms and enhance the ionic conductivity. A noteworthy characteristic of these electrolytes is their high electrochemical stability, with wide potential windows in solutions (up to 3.0 V), similar to other compounds used in batteries.[19,48−50] In addition, the structural, spectroscopic, thermal stability, electrochemical stability, and ionic conductivity data presented here provide a rich data set for data-driven approaches that could enable discovery of optimized *closo*-borate electrolytes.[51,52] Looking ahead, the synergy of high thermal stability, weak coordination, structural disorder, and superior Li^+ conductivity in perhalogenated *closo*-dodecaborates establishes them as a platform for next-generation electrolytes in advanced batteries and electrochemical devices.

■ ASSOCIATED CONTENT

Supporting Information

The Supporting Information is available free of charge at https://pubs.acs.org/doi/10.1021/acs.chemmater.6c00218.

$LI_2B_{12}BR_{12}$ *Fm*$\bar{3}$*m* 800 K (CIF)
$LI_2B_{12}BR_{12}$ Pn$\bar{3}$ 500 K (CIF)
$LI_2B_{12}BR_{12}$ Pn$\bar{3}$ 700 K (CIF)
$LI_2B_{12}CL_{12}$ *Fm*$\bar{3}$*m* 810 K (CIF)
$LI_2B_{12}CL_2$ *Pn*$\bar{3}$ 400 K (CIF)
$LI_2B_{12}CL_2$ *Pn*$\bar{3}$ RT (CIF)
$LI_2B_{12}F_{12}$ *Cmca* 475 K (CIF)
$LI_2B_{12}F_{12}$ *Cmca* RT (CIF)
$LI_2B_{12}I_{12}$ *Pn*$\bar{3}$ 500 K (CIF)
Additional details on X-ray powder diffraction measurements, Rietveld refinements, FTIR, Raman, TGA, RGA, and DSC measurements (PDF)

■ AUTHOR INFORMATION

Corresponding Author

Vitalie Stavila − *Sandia National Laboratories, Livermore, California 94551, United States;* orcid.org/0000-0003-0981-0432; Email: vnstavi@sandia.gov

Authors

Agnieszka Prus − *Center of New Technology, University of Warsaw, Warsaw 02-097, Poland; Sandia National Laboratories, Livermore, California 94551, United States;* orcid.org/0000-0002-2035-4733

Hui Wu − *NIST Center for Neutron Research, National Institute of Standards and Technology, Gaithersburg, Maryland 20899-6102, United States*

Wei Zhou − *NIST Center for Neutron Research, National Institute of Standards and Technology, Gaithersburg, Maryland 20899-6102, United States*

Austin Bhandarkar − *Sandia National Laboratories, Livermore, California 94551, United States*

Joseph A. Teprovich Jr − *California State University Northridge, Northridge, California 91330, United States;* orcid.org/0000-0002-7285-4844

Karol J. Fijalkowski − *Center of New Technology, University of Warsaw, Warsaw 02-097, Poland*

A. Alec Talin − *Sandia National Laboratories, Livermore, California 94551, United States;* orcid.org/0000-0002-1102-680X

Complete contact information is available at: https://pubs.acs.org/10.1021/acs.chemmater.6c00218

Author Contributions

The manuscript was written through the contributions of all authors. All authors have given approval to the final version of the manuscript.

Notes

Certain commercial equipment, instruments, or materials are identified in this document. Such identification does not imply recommendation or endorsement by the National Institute of Standards and Technology, nor does it imply that the products identified are necessarily the best available for the purpose. The authors declare no competing financial interest.

■ ACKNOWLEDGMENTS

A.P. thanks Piotr J. Leszczyśnki for his help with training and valuable technical discussions. The authors also acknowledge Dr. Marissa Wood for support with the high-temperature electrochemical measurements. Sandia National Laboratories is a multimission laboratory managed and operated by National Technology & Engineering Solutions of Sandia, LLC (NTESS), a wholly owned subsidiary of Honeywell International Inc., for the U.S. Department of Energy's National Nuclear Security Administration (DOE/NNSA) under contract DE-NA0003525. This work was partially supported by the U.S. Department of Energy, Office of Science, Office of Basic Energy Sciences, under Grant DE-SC0021070. "This work was also supported by the Sandia Laboratory Directed Research and Development (LDRD) Program. J.T. would like to acknowledge the LEAPS-MPS program of the National Science Foundation under Grant No. 2137973. This research was partially funded by The Polish National Science Centre within the project Sonata Bis 8 (UMO/2018/30/E/ST5/00854). The views and opinions of the authors expressed herein do not necessarily state or reflect those of the United States Government or any agency thereof. Neither the United States Government nor any agency thereof, nor any of their employees, makes any warranty, expressed or implied, or assumes any legal liability or responsibility for the accuracy,

completeness, or usefulness of any information, apparatus, product, or process disclosed, or represents that its use would not infringe privately owned rights.

REFERENCES

(1) Tang, W. S.; Dimitrievska, M.; Stavila, V.; Zhou, W.; Wu, H.; Talin, A. A.; Udovic, T. J. Order-Disorder Transitions and Superionic Conductivity in the Sodium *Nido*-Undeca(Carba)Borates. *Chem. Mater.* **2017**, *29*, 10496−10509.

(2) Hansen, B. R. S.; Paskevicius, M.; Jørgensen, M.; Jensen, T. R. Halogenated Sodium-Closo-Dodecaboranes as Solid-State Ion Conductors. *Chem. Mater.* **2017**, *29*, 3423−3430.

(3) Hansen, B. R. S.; Paskevicius, M.; Li, H. W.; Akiba, E.; Jensen, T. R. Metal Boranes: Progress and Applications. *Coord. Chem. Rev.* **2016**, *323*, 60−70.

(4) Paskevicius, M.; Hansen, B. R. S.; Jørgensen, M.; Richter, B.; Jensen, T. R. Multifunctionality of Silver *Closo*-Boranes. *Nat. Commun.* **2017**, *8*, No. 15136.

(5) Simonyan, H.; Zhong, L.; Green, M. M.; Movsesyan, K.; Fraire, A.; Ward, P. A.; Lau, K. C.; Teprovich, J. A. Solvation Environment and Interface Dynamics of $Li_2B_{12}H_{12}$ and $Li_2B_{12}F_{12}$ Electrolytes Uncovered by Theory and Operando Optical and FTIR Spectroelectrochemistry. *ACS Appl. Mater. Interfaces* **2024**, *16*, 70028−70037.

(6) Grill, J.; Steensen, S. K.; Castro, D. L. Q.; Castelli, I. E.; Popovic-Neuber, J. Solid-State Inorganic Electrolytes for next Generation Potassium Batteries. *Commun. Mater.* **2024**, *5*, No. 127.

(7) Brighi, M.; Murgia, F.; Černý, R. Closo-Hydroborate Sodium Salts as an Emerging Class of Room-Temperature Solid Electrolytes. *Cell Rep. Phys. Sci.* **2020**, *1*, No. 100217.

(8) Sau, K.; Takagi, S.; Ikeshoji, T.; Kisu, K.; Sato, R.; dos Santos, E. C.; Li, H.; Mohtadi, R.; Orimo, S. I. Unlocking the Secrets of Ideal Fast Ion Conductors for All-Solid-State Batteries. *Commun. Mater.* **2024**, *5*, No. 122.

(9) Huang, J.; Wu, K.; Xu, G.; Wu, M.; Dou, S.; Wu, C. Recent progress and strategic perspectives of inorganic solid electrolytes: fundamentals, modifications, and applications in sodium metal batteries. *Chem. Soc. Rev.* **2023**, *52*, 4933−4995.

(10) Udovic, T. J.; Matsuo, M.; Unemoto, A.; Verdal, N.; Stavila, V.; Skripov, A. V.; Rush, J. J.; Takamura, H.; Orimo, S. I. Sodium Superionic Conduction in $Na_2B_{12}H_{12}$. *Chem. Commun.* **2014**, *50*, 3750−3752.

(11) Moury, R.; Łodziana, Z.; Remhof, A.; Duchêne, L.; Roedern, E.; Gigantea, A.; Hagemann, H. Pressure-induced phase transitions in Na2B12H12, structural investigation on a candidate for solid state electrolyte. *Acta Crystallogr., Sect. B: Struct. Sci., Cryst. Eng. Mater.* **2019**, *75*, 406−413.

(12) Teprovich, J. A.; Colón-Mercado, H.; Washington, A. L.; Ward, P. A.; Greenway, S.; Missimer, D. M.; Hartman, H.; Velten, J.; Christian, J. H.; Zidan, R. Bi-Functional $Li_2B_{12}H_{12}$ for Energy Storage and Conversion Applications: Solid-State Electrolyte and Luminescent down-Conversion Dye. *J. Mater. Chem. A* **2015**, *3*, 22853−22859.

(13) Verdal, N.; Her, J. H.; Stavila, V.; Soloninin, A. V.; Babanova, O. A.; Skripov, A. V.; Udovic, T. J.; Rush, J. J. Complex High-Temperature Phase Transitions in $Li_2B_{12}H_{12}$ and $Na_2B_{12}H_{12}$. *J. Solid State Chem.* **2014**, *212*, 81−91.

(14) Maltsev, A. P.; Chepkasov, I. V.; Oganov, A. R. Order-Disorder Phase Transition and Ionic Conductivity in a $Li_2B_{12}H_{12}$ Solid Electrolyte. *ACS Appl. Mater. Interfaces* **2023**, *15*, 42511−42519.

(15) Payandeh, S.; Asakura, R.; Avramidou, P.; Rentsch, D.; Łodziana, Z.; Černý, R.; Remhof, A.; Battaglia, C. Nido-Borate/Closo-Borate Mixed-Anion Electrolytes for All-Solid-State Batteries. *Chem. Mater.* **2020**, *32*, 1101−1110.

(16) dos Santos, E.; Sato, R.; Kisu, K.; Sau, K.; Jia, X.; Yang, F.; Orimo, S.-i.; Li, H. Explore the Ionic Conductivity Trends on $B_{12}H_{12}$ Divalent Closo-Type Complex Hydride Electrolytes. *Chem. Mater.* **2023**, *35*, 5996−6004.

(17) Zhou, R.; Luo, K.; Fei, L.; An, Q. Unraveling Superionic Conductivity in $Na_2B_{12}H_{12}$: Molecular Dynamics Study of Phase Transition, Anion Reorientation, and Ionic Conductivity via Machine Learning Force Field. *ACS Electrochem.* **2025**, *1*, 143−152.

(18) Simon, P.; Gogotsi, Y. Perspectives for Electrochemical Capacitors and Related Devices. *Nat. Mater.* **2020**, *19*, 1151−1163.

(19) Quartarone, E.; Mustarelli, P. Electrolytes for Solid-State Lithium Rechargeable Batteries: Recent Advances and Perspectives. *Chem. Soc. Rev.* **2011**, *40*, 2525−2540.

(20) Wang, X.; Salari, M.; Jiang, D.-e.; Varela, J. C.; Anasori, B.; Wesolowski, D. J.; Dai, S.; Grinstaff, M. W.; Gogotsi, Y. Electrode Material−Ionic Liquid Coupling for Electrochemical Energy Storage. *Nat. Rev. Mater.* **2020**, *5*, 787−808.

(21) Chen, X.; Vereecken, P. M. Solid and Solid-Like Composite Electrolyte for Lithium Ion Batteries: Engineering the Ion Conductivity at Interfaces. *Adv. Mater. Interfaces* **2019**, *6*, No. 1800899.

(22) Kweon, K.; Varley, J.; Shea, P.; Adelstein, N.; Mehta, P.; Udovic, T. J.; Stavila, V.; Wood, B. Structural, Chemical, and Dynamical Frustration in Superionic Closo-Borane Solid Electrolytes. *Chem. Mater.* **2017**, *29*, 9142−9153.

(23) Varley, J. B.; Kweon, K.; Mehta, P.; Shea, P.; Heo, T. W.; Udovic, T. J.; Stavila, V.; Wood, B. C. Understanding Ionic Conductivity Trends in Polyborane Solid Electrolytes from Ab Initio Molecular Dynamics. *ACS Energy Lett.* **2017**, *2*, 250−255.

(24) Tang, W. S.; Unemoto, A.; Zhou, W.; Stavila, V.; Matsuo, M.; Wu, H.; Orimo, S. I.; Udovic, T. J. Unparalleled Lithium and Sodium Superionic Conduction in Solid Electrolytes with Large Monovalent Cage-like Anions. *Energy Environ. Sci.* **2015**, *8*, 3637−3645.

(25) Tang, W. S.; Matsuo, M.; Wu, H.; Stavila, V.; Zhou, W.; Talin, A. A.; Soloninin, A. V.; Skoryunov, R. V.; Babanova, O. A.; Skripov, A. V.; Unemoto, A.; Orimo, S. I.; Udovic, T. J. Liquid-Like Ionic Conduction in Solid Lithium and Sodium Monocarba-Closo-Decaborates Near or at Room Temperature. *Adv. Energy Mater.* **2016**, *6*, No. 1502237.

(26) Jørgensen, M.; Shea, P. T.; Tomich, A. W.; Varley, J. B.; Bercx, M.; Lovera, S.; Černý, R.; Zhou, W.; Udovic, T. J.; Lavallo, V.; Jensen, T. R.; Wood, B. C.; Stavila, V. Understanding Superionic Conductivity in Lithium and Sodium Salts of Weakly Coordinating Closo-Hexahalocarbaborate Anions. *Chem. Mater.* **2020**, *32*, 1475−1487.

(27) Toby, B. H.; von Dreele, R. B. GSAS-II: The Genesis of a Modern Open-Source All-Purpose Crystallography Software Package. *J. Appl. Crystallogr.* **2013**, *46*, 544−549.

(28) Giannozzi, P.; Andreussi, O.; Brumme, T.; Bunau, O.; Nardelli, M. B.; Calandra, M.; Car, R.; Cavazzoni, C.; Ceresoli, D.; Cococcioni, M.; Colonna, N.; Carnimeo, I.; Dal Corso, A.; De Gironcoli, S.; Delugas, P.; Distasio, R. A.; Ferretti, A.; Floris, A.; Fratesi, G.; Fugallo, G.; Gebauer, R.; Gerstmann, U.; Giustino, F.; Gorni, T.; Jia, J.; Kawamura, M.; Ko, H.-Y.; Kokalj, A.; Küçükbenli, E.; Lazzeri, M.; Marsili, M.; Marzari, N.; Mauri, F.; Nguyen, N. L.; Nguyen, H.-V.; Otero-De-La-Roza, A.; Paulatto, L.; Poncé, S.; Rocca, D.; Sabatini, R.; Santra, B.; Schlipf, M.; Seitsonen, A. P.; Smogunov, A.; Timrov, I.; Thonhauser, T.; Umari, P.; Vast, N.; Wu, X.; Baroni, S. Advanced Capabilities for Materials Modelling with Quantum ESPRESSO. *J. Phys.: Condens. Matter* **2017**, *29*, No. 465901.

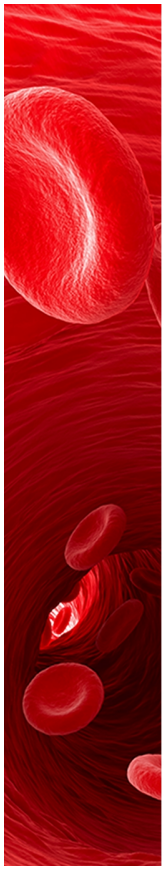
(29) Baroni, S.; De Gironcoli, S.; Dal Corso, A.; Giannozzi, P. Phonons and Related Properties of Extended Systems from Density-Functional Perturbation Theory. *Rev. Mod. Phys.* **2001**, *73*, 515−562.

(30) Her, J. H.; Yousufuddin, M.; Zhou, W.; Jalisatgi, S. S.; Kulleck, J. G.; Zan, J. A.; Hwang, S. J.; Bowman, R. C.; Udovic, T. J. Crystal Structure of $Li_2B_{12}H_{12}$: A Possible Intermediate Species in the Decomposition of $LiBH_4$. *Inorg. Chem.* **2008**, *47*, 9757−9759.

(31) Bukovsky, E. V.; Peryshkov, D. V.; Wu, H.; Zhou, W.; Tang, W. S.; Jones, W. M.; Stavila, V.; Udovic, T. J.; Strauss, S. H. Comparison of the Coordination of $B_{12}F_{12}^{2-}$, $B_{12}Cl_{12}^{2-}$, and $B_{12}H_{12}^{2-}$ to Na^+ in the Solid State: Crystal Structures and Thermal Behavior of $Na_2(B_{12}F_{12})$, $Na_2(H_2O)_4(B_{12}F_{12})$, $Na_2(B_{12}Cl_{12})$, and $Na_2(H_2O)_6(B_{12}Cl_{12})$. *Inorg. Chem.* **2017**, *56*, 4369−4379.

https://doi.org/10.1021/acs.chemmater.6c00218
Chem. Mater. 2026, 38, 5960−5972

(32) Tiritiris, I.; Schleid, T. The Crystal Structure of Solvent-Free Silver Dodecachloro-*Closo*-Dodecaborate $Ag_2[B_{12}Cl_{12}]$ from Aqueous Solution. *Z. Anorg. Allg. Chem.* **2003**, *629*, 581−583.
(33) Dimitrievska, M.; Wu, H.; Stavila, V.; Babanova, O. A.; Skoryunov, R. V.; Soloninin, A. V.; Zhou, W.; Trump, B. A.; Andersson, M. S.; Skripov, A. V.; Udovic, T. J. Structural and Dynamical Properties of Potassium Dodecahydro-Monocarba-*Closo*-Dodecaborate: $KCB_{11}H_{12}$. *J. Phys. Chem. C* **2020**, *124*, 17992−18002.
(34) Udovic, T. J.; Matsuo, M.; Tang, W. S.; Wu, H.; Stavila, V.; Soloninin, A. V.; Skoryunov, R. V.; Babanova, O. A.; Skripov, A. V.; Rush, J. J.; Unemoto, A.; Takamura, H.; Orimo, S. I. Exceptional Superionic Conductivity in Disordered Sodium Decahydro-*Closo*-Decaborate. *Adv. Mater.* **2014**, *26*, 7622−7626.
(35) Tiritiris, I. Untersuchungen Zu Reaktivität, Aufbau Und Dynamik von Salzartigen, Ph.D. Thesis; Institut für Anorganische Chemie der Universität: Stuttgart, Germany, 2003.
(36) Tiritiris, I.; Barei, K. U.; Schleid, T. Investigations on the Polymorphism of the Cesium Dodecahalogeno-*Closo*-Dodecaborates $Cs_2[B_{12}X_{12}]$ (X = Cl-I). *Z. Naturforsch. B* **2020**, *75*, 777−790.
(37) Leites, L. A.; Bukalov, S. S.; Nesmeyanov, A. N.; Kurbakova, A. P.; Kaganski, M. M.; Gaft, Y. L.; Kuznetsov, N. T.; Zakharova, I. A.; Kurnakov, N. S. Vibrational Spectra of Icosahedral Closoborate Anions $B_{12}X_{12}^{2-}$ (X = H, D, CI, Br, I). *Spectrochim. Acta, Part A* **1982**, *38*, 1047−1056.
(38) Sharma, M.; Sethio, D.; Lawson Daku, L. M.; Hagemann, H. Theoretical Study of Halogenated $B_{12}H_nX_{(12-n)}^{2-}$ (X = F, Cl, Br). *J. Phys. Chem. A* **2019**, *123*, 1807−1813.
(39) Hehn, J. D.; Rodenburg, H. P.; Lazemi, M.; Verschoor, J. C.; Perxés Perich, M.; Sundermann, M.; Gretarsson, H.; van der Hoeven, J. E. S.; de Groot, F. M. F.; de Jongh, P. E.; Ngene, P. Enhanced Ionic Conductivity and Electrochemical Properties of $Li_2B_{12}H_{12}/ZrO_2$ Nanocomposites for All-Solid-State Lithium Metal Batteries. *ACS Appl. Mater. Interfaces* **2025**, *17*, 33824−33833.
(40) Jin, M.; Xu, D.; Su, Z.; Liu, R.; Xiang, M.; Cheng, Y.; Wu, R.; Guo, Y. Hydridoborate-Based Solid Electrolytes for All-Solid-State Batteries. *Adv. Mater.* **2016**, No. e07809, DOI: 10.1002/adma.202507809.
(41) Lu, Z. W.; Kang, J. X.; Qiu, P. T.; Chen, X. N. Hydridoborate-Based Solid-State Electrolytes for Sodium Metal Batteries. *Batteries Supercaps* **2025**, *8*, No. e202400636.
(42) Liu, H.; Zhou, X.; Ye, M.; Shen, J. Ion Migration Mechanism Study of Hydroborate/Carborate Electrolytes for All-Solid-State Batteries. *Electrochem. Energy Rev.* **2023**, *6*, No. 31.
(43) Green, M.; Kaydanik, K.; Orozco, M.; Hanna, L.; Marple, M. A. T.; Fessler, K. A. S.; Jones, W. B.; Stavila, V.; Ward, P. A.; Teprovich, J. A. Closo-Borate Gel Polymer Electrolyte with Remarkable Electrochemical Stability and a Wide Operating Temperature Window. *Adv. Sci.* **2022**, *9*, No. 2106032.
(44) Zhang, Z.; Nazar, L. F. Exploiting the Paddle-Wheel Mechanism for the Design of Fast Ion Conductors. *Nat. Rev. Mater.* **2022**, *7*, 389−405.
(45) Kim, S.; Kisu, K.; Takagi, S.; Oguchi, H.; Orimo, S. I. Complex Hydride Solid Electrolytes of the $Li(CB_9H_{10})$-$Li(CB_{11}H_{12})$ Quasi-Binary System: Relationship between the Solid Solution and Phase Transition, and the Electrochemical Properties. *ACS Appl. Energy Mater.* **2020**, *3*, 4831−4839.
(46) Kim, S.; Oguchi, H.; Toyama, N.; Sato, T.; Takagi, S.; Otomo, T.; Arunkumar, D.; Kuwata, N.; Kawamura, J.; Orimo, S. A Complex Hydride Lithium Superionic Conductor for High-Energy-Density All-Solid-State Lithium Metal Batteries. *Nat. Commun.* **2019**, *10*, No. 1081.
(47) Tang, W. S.; Yoshida, K.; Soloninin, A. V.; Skoryunov, R. V.; Babanova, O. A.; Skripov, A. V.; Dimitrievska, M.; Stavila, V.; Orimo, S. I.; Udovic, T. J. Stabilizing Superionic-Conducting Structures via Mixed-Anion Solid Solutions of Monocarba-*Closo*-Borate Salts. *ACS Energy Lett.* **2016**, *1*, 659−664.
(48) Korthauer, R. *Lithium-Ion Batteries: Basics and Applications*; Springer Berlin Heidelberg, 2018; p 413.
(49) Lapp, A. S.; Merrill, L. C.; Wygant, B. R.; Ashby, D. S.; Bhandarkar, A. S.; Zhang, A. C.; Fuller, E. J.; Harrison, K. L.; Lambert, T. N.; Talin, A. A. Room-Temperature Pseudo-Solid-State Iron Fluoride Conversion Battery with High Ionic Conductivity. *ACS Appl. Mater. Interfaces* **2023**, *15*, 893−902.
(50) Asakura, R.; Duchêne, L.; Kühnel, R. B.; Remhof, A.; Hagemann, H.; Battaglia, C. *ACS Appl. Energy Mater.* **2019**, *2*, 6924−6930.
(51) Dutra, A. C. C.; Goldmann, B. A.; Islam, M. S.; Dawson, J. A. Understanding solid-state battery electrolytes using atomistic modelling and machine learning. *Nat. Rev. Mater.* **2025**, *10*, 566−583.
(52) Xie, S. R.; Honrao, S. J.; Lawson, J. W. High-Throughput Screening of Li Solid-State Electrolytes with Bond Valence Methods and Machine Learning. *Chem. Mater.* **2024**, *36*, 9320−9329.


CAS BIOFINDER DISCOVERY PLATFORM™
CAS BIOFINDER HELPS YOU FIND YOUR NEXT BREAKTHROUGH FASTER
Navigate pathways, targets, and diseases with precision
Explore CAS BioFinder
CAS
A division of the American Chemical Society